The 15th International Symposium on Magnetic Bearings, August 3-6, 2016, Mojiko Hotel, Kitakyushu, Japan

ISMB15

Flux-Linkage Model Including Cross-Saturation for a Bearingless Synchronous Reluctance Motor

Seppo E. SAARAKKALA*, Maksim SOKOLOV*, Victor MUKHERJEE*, Jenni PIPPURI**, Kari TAMMI***, Anouar BELAHCEN* and Marko HINKKANEN*

* Aalto University School of Electrical Engineering
P.O. Box 13000, FI-00076 Aalto, Finland
** VTT Technical Research Centre of Finland
P.O. Box 1000, FI-02044 VTT, Finland
*** Aalto University School of Engineering
P.O. Box 14100, FI-00076 Aalto, Finland

Abstract

This paper deals with magnetic modeling of a bearingless synchronous reluctance motor. The motor under consideration includes two separate sets of three-phase windings, one for torque production and the other one for radial-force production. This paper demonstrates by means of finite-element analysis, that it is unrealistic to assume the two three-phase windings to be decoupled from one another. Instead, it is shown that especially the torque-producing winding currents affect to the operation of the radial-force producing winding. A simple nine-parameter explicit-function based magnetic model is proposed to model the cross-saturation between the two winding sets. The effectiveness of the proposed magnetic model is demonstrated by applying it together with model-based torque and radial-force controllers.

Key words : Magnetic model, Radial-force production, Bearingless motor, Magnetic saturation

1. Introduction

In recent years, bearingless machines have received increasing attention as an alternative to conventional mechanical bearings, especially in high-speed applications (Mitterhofer et al., 2014). Bearingless drives incorporate the functions of active magnetic bearings and electrical machine in one unit, which reduces the size, complexity and price of the system (Chiba et al., 1994). Several motor topologies have been proposed in the literature to be used as bearingless motors, e.g. (Chiba et al., 1994; Gruber et al., 2009; Nussbaumer et al., 2011; Asama et al., 2013). Particularly in lower speed and higher power applications, the bearingless synchronous reluctance motor (BSyRM) is an attractive alternative. The advantages of BSyRM include, e.g., that it neither needs the permanent magnets (PMs) placed in the rotor, like the PM machines do, nor it produces additional losses because of the rotor currents, like the induction machines do. However, the synchronous reluctance motors are often operated with relatively high currents, which means that the magnetic circuit of the motor is saturated.

The BSyRM considered in this paper includes two separate sets of three-phase windings. One winding set is for production of the shaft torque and is referred to as a main winding. The second winding set is for production of the radial force for stable levitation of the rotor and is referred to as a suspension winding. For independent and rapid production of the required torque and force, the performance of the current (or flux linkage) control loop is especially important since it has a direct influence on the overall stability of the system. Moreover, the current-control loop sets the dynamic limitations for the outer control loops, i.e., the speed-control loop and the radial-position control loop. Thus, it is important to know the magnetic model of the motor in detail to be able to establish accurate model-based torque and force-control loops (Harnefors and Nee, 1998; Briz et al., 1999; Hinkkanen et al., 2016). In an ideal case, the dynamics of the two three-phase windings are decoupled, when the rotor is centric (Chiba et al., 1994). This assumption is used, e.g., in study by (Xu et al., 2013), where the torque and force productions are separately designed. However, it is demonstrated by several studies that heavy cross-saturation appear in conventional SyRMs, e.g. (Yamamoto et al., 2007). Thus, it is realistic to assume that similar cross-saturation behaviour appear also in BSyRMs, meaning that the two windings may be coupled, even if the rotor is centric.

The main contributions of this paper can be summarized as follows: 1) The saturation characteristics of BSyRM are analyzed in more detail than in previous studies, e.g. (Michioka et al., 1996), including self-saturation and cross-saturation; 2) a nine-parameter explicit function is proposed to model the cross-saturation between the main winding and the additional winding; 3) Comparison between explicit-function based and constant-parameter current-controller designs are carried out by means of simulations.

2. System Model

As depicted in Fig. 1, the studied BSyRM has a 4-pole multi-flux-barrier rotor (Mukherjee et al., 2015). A 4-pole main winding for the torque production and a 2-pole suspension winding for the radial-force production are sinusoidally distributed in the stator. In the following, the system model is analyzed in synchronous coordinates (rotating at twice the shaft speed ω_M).

The voltage equations of the main winding (marked with subscript m) and the suspension winding (marked with subscript s) are (Chiba et al., 1994)

$$\frac{\mathrm{d}\boldsymbol{\psi}_\mathrm{m}}{\mathrm{d}t} = \boldsymbol{u}_\mathrm{m} - R_\mathrm{m}\boldsymbol{i}_\mathrm{m} - 2\omega_\mathrm{M}\boldsymbol{J}\boldsymbol{\psi}_\mathrm{m}, \qquad \frac{\mathrm{d}\boldsymbol{\psi}_\mathrm{s}}{\mathrm{d}t} = \boldsymbol{u}_\mathrm{s} - R_\mathrm{s}\boldsymbol{i}_\mathrm{s} - \omega_\mathrm{M}\boldsymbol{J}\boldsymbol{\psi}_\mathrm{s} \tag{1}$$

respectively, where $\boldsymbol{J} = \left[\begin{smallmatrix} 0 & -1 \\ 1 & 0 \end{smallmatrix}\right]$ and the voltage vectors are defined as $\boldsymbol{u}_\mathrm{m} = \begin{bmatrix} u_\mathrm{md} & u_\mathrm{mq} \end{bmatrix}^\mathrm{T}$ and $\boldsymbol{u}_\mathrm{s} = \begin{bmatrix} u_\mathrm{sd} & u_\mathrm{sq} \end{bmatrix}^\mathrm{T}$. The current vectors and the flux-linkage vectors are defined similarly. The resistances of the windings are R_m and R_s, respectively. The angular speed of the shaft is defined as $\omega_\mathrm{M} = \mathrm{d}\vartheta_\mathrm{M}/\mathrm{d}t$, where ϑ_M is the angular position of the shaft.

With linear magnetics, the flux linkages of the main winding $\boldsymbol{\psi}_\mathrm{m}$ and the suspension winding $\boldsymbol{\psi}_\mathrm{s}$ can be represented in matrix format (Chiba et al., 1994):

$$\underbrace{\begin{bmatrix} \boldsymbol{\psi}_\mathrm{m} \\ \boldsymbol{\psi}_\mathrm{s} \end{bmatrix}}_{\boldsymbol{\psi}} = \underbrace{\begin{bmatrix} \boldsymbol{L}_\mathrm{m} & \boldsymbol{M} \\ \boldsymbol{M}^\mathrm{T} & \boldsymbol{L}_\mathrm{s} \end{bmatrix}}_{\boldsymbol{L}_\Sigma} \underbrace{\begin{bmatrix} \boldsymbol{i}_\mathrm{m} \\ \boldsymbol{i}_\mathrm{s} \end{bmatrix}}_{\boldsymbol{i}}, \qquad \boldsymbol{L}_\mathrm{m} = \begin{bmatrix} L_\mathrm{d} & 0 \\ 0 & L_\mathrm{q} \end{bmatrix}, \qquad \boldsymbol{L}_\mathrm{s} = \begin{bmatrix} L_\mathrm{s} & 0 \\ 0 & L_\mathrm{s} \end{bmatrix}, \qquad \boldsymbol{M} = \begin{bmatrix} M'_\mathrm{d} i & -M'_\mathrm{d} j \\ M'_\mathrm{q} j & M'_\mathrm{q} i \end{bmatrix} \tag{2}$$

where L_d, L_q, L_s are inductances and M'_d, M'_q are radial-force constants. The rotor displacements in rotating coordinates are denoted as i and j, cf. Figs. 1(a) and 1(c). It can be noted that the cross coupling between the main winding and the suspension winding exists only when i and j are nonzero, i.e., when the rotor is not centric.

3. FEA Results and Magnetic Model

It has been demonstrated in several studies, that it is unrealistic to assume a linear magnetic circuit in SyRMs and BSyRMs (Michioka et al., 1996; Yamamoto et al., 2007). Thus, instead of using (2), the flux linkages are modeled as a function of currents, i.e. $\boldsymbol{\psi} = \boldsymbol{\psi}(\boldsymbol{i})$, in the following section. The calculation is based on static finite-element analysis (FEA) in pre-selected operating points and both the windings are current supplied in FEA. The rotor is assumed to be centric and the angle of the rotor is kept zero in every operating points, cf. Figs. 1(a) and 1(c). However, the current angles are always varied between different FE solutions. As an example, Figs. 1(a) and 1(c) show the pre-defined current vectors $\boldsymbol{i}_\mathrm{m}$ and $\boldsymbol{i}_\mathrm{s}$ for two operating points and Figs. 1(b) and 1(d) show the corresponding magnetic-field solutions. When the no-load operating point [Fig. 1(a)] is compared with the loaded one [Fig. 1(c)], it can be seen that the saturation state of the motor is different. Furthermore, Fig. 1(a) clearly demonstrates that the flux density in the airgap is unbalanced, which means that the radial force is produced. The flux linkages $\boldsymbol{\psi}_\mathrm{m}$ and $\boldsymbol{\psi}_\mathrm{s}$ of both windings are calculated from the magnetic-field solution by using the post-processing algorithms of FE software. In addition to the flux linkages, the FE software computes values of the electromagnetic torque T_M and the radial-force components F_x and F_y.

The main-winding current amplitude is varied between 2.5 A and 45.9 A (peak-to-peak) and the suspension-winding current amplitude is varied between 0.35 A and 3.18 A (peak-to-peak). Based on the FEA results, the maximum torque of the motor is 29 Nm and the maximum amplitude of the radial force is 2000 N within these current regions.

3.1. Flux Linkages as Function of Main-Winding Current

Based on the FEA results, it was found out that the main-winding d-axis inductance L_d remains almost constant (within 6% variation) throughout the whole operating region. As an example, Fig. 2(a) shows the main-winding d-axis flux linkage ψ_md as a function of i_md and i_mq. It can be seen that practically neither the self-saturation nor the cross-saturation exist, meaning that L_d can be assumed to be constant. On the other hand, there is clear self-saturation between

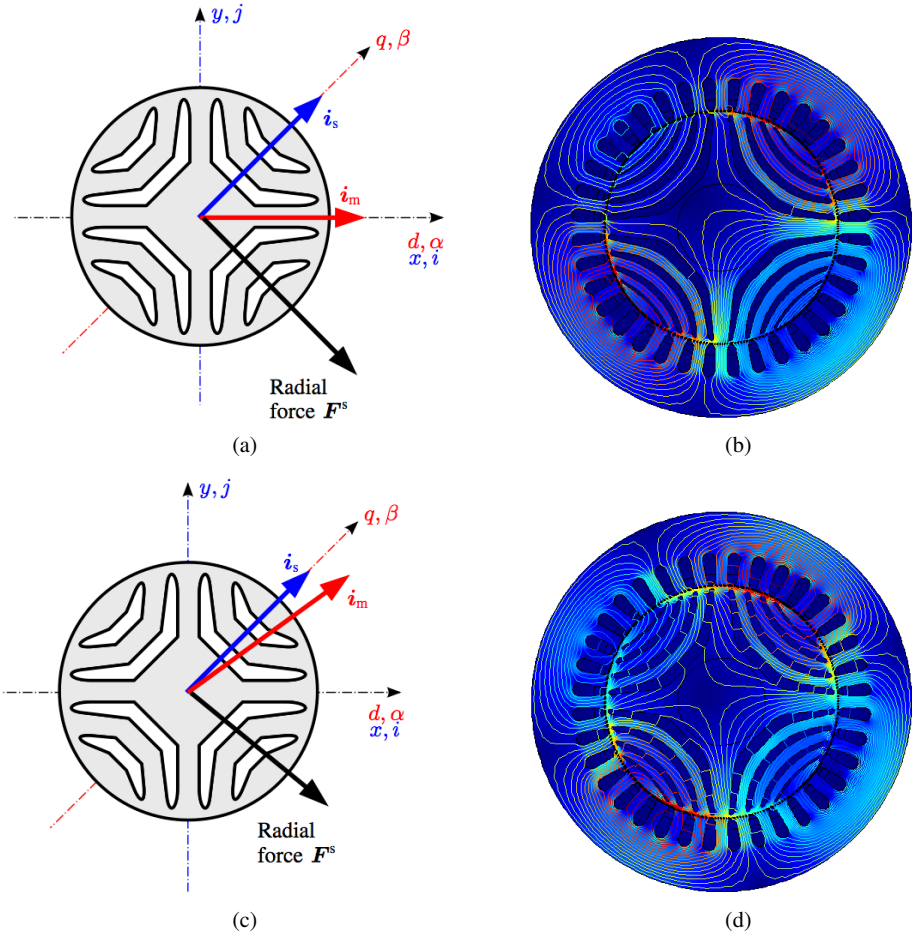

Fig. 1 (a), (c): Current vectors $\boldsymbol{i}_\mathrm{m}$ and $\boldsymbol{i}_\mathrm{s}$ together with radial-force vector for two operating points; and (b), (d): the corresponding magnetic-field solutions computed with FE software. The stationary coordinates of the main and suspension windings are marked with (α, β) and (x, y), respectively. Similarly, the rotating coordinates of the main and suspension windings are marked with (d, q) and (i, j), respectively.

i_mq and ψ_mq, as demonstrated in Fig. 2(b). Moreover, it was found out that there is also clear cross-saturation between the main-winding q-axis current component i_mq and the suspension-winding flux linkages ψ_sd and ψ_sq, meaning that the suspension-winding inductance L_s cannot be considered constant. Fig. 2(c) demonstrates this phenomenon.

3.2. Flux Linkages as Function of Suspension-Winding Current

Based on the FEA results, it was found out that the neither the self-saturation nor the cross-saturation exist between the suspension-winding currents and suspension-winding flux linkages, as demonstrated in Fig. 3(c). Thus, it can be assumed that the suspension-winding inductance L_s depend only on the main-winding currents. Furthermore, it was found out that the cross-saturation between the suspension-winding currents and the main-winding flux linkages is minimal, as demonstrated in Figs. 3(a) and 3(b). This means that it can be assumed that the main-winding inductances L_d and L_q do not depend on the the suspension-winding currents.

3.3. Force Constants as Function of Currents

The radial-force vector is defined in stationary xy coordinates as (Michioka et al., 1996)

$$\boldsymbol{F}^\mathrm{s} = \begin{bmatrix} F_\mathrm{x} \\ F_\mathrm{y} \end{bmatrix} = \mathrm{e}^{\vartheta_\mathrm{M} \boldsymbol{J}} \begin{bmatrix} M'_\mathrm{d} i_\mathrm{md} & M'_\mathrm{q} i_\mathrm{mq} \\ M'_\mathrm{q} i_\mathrm{mq} & -M'_\mathrm{d} i_\mathrm{md} \end{bmatrix} \boldsymbol{i}_\mathrm{s} \tag{3}$$

Because all the current components as well as the radial-force components are known after each FE simulation, the radial-force constants can be calculated as function of currents in each operating point using (3). Based on the calculated results, it was found out that the radial-force constants M'_d and M'_q highly depend on the main-winding currents. It was also found out that the M'_d dominates the radial-force production. Variation in the q-axis force-constant M'_q has only minor effects to

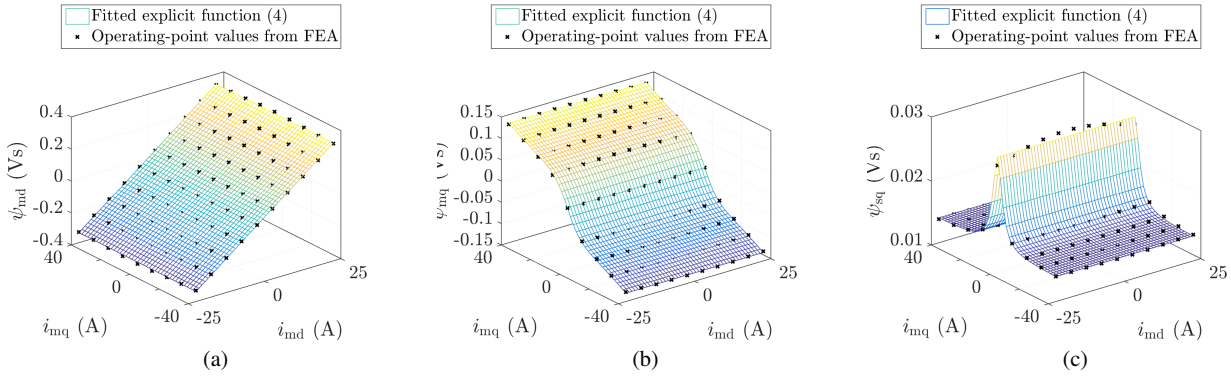

Fig. 2 Flux linkages as function of main-winding currents, calculated with the magnetic model (4): (a) $\psi_{md}(i_{md}, i_{mq})$; (b) $\psi_{mq}(i_{md}, i_{mq})$; and (c) $\psi_{sq}(i_{md}, i_{mq})$. The FEA data points are shown as black crosses.

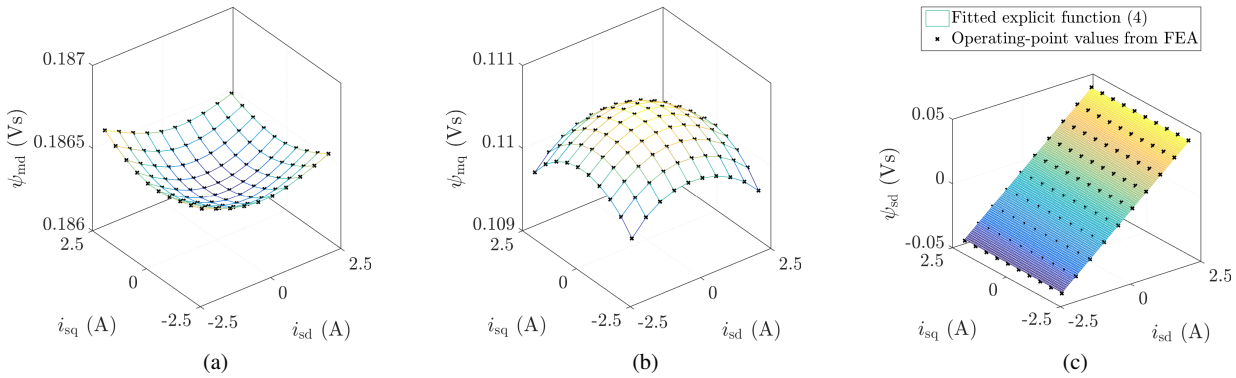

Fig. 3 Flux linkages as function of suspension-winding currents: (a) $\psi_{md}(i_{sd}, i_{sq})$ is obtained from FEA; (b) $\psi_{mq}(i_{sd}, i_{sq})$ is obtained from FEA; and (c) $\psi_{sd}(i_{sd}, i_{sq})$ is obtained from the magnetic model (4). The FEA data points are shown as black crosses.

the produced radial force.

3.4. Explicit-Function Based Magnetic Model

Based on the observations made in the previous three sections, the following magnetic model is proposed for the BSyRM

$$\psi_{md}(i_{md}) = L_d i_{md}, \qquad \psi_{mq}(i_{mq}) = L_q(i_{mq}) i_{mq}, \qquad \psi_{sd}(i_{mq}, i_{sd}) = L_s(i_{mq}) i_{sd}, \qquad \psi_{sq}(i_{mq}, i_{sq}) = L_s(i_{mq}) i_{sq}$$
$$L_q(i_{mq}) = L_{q,0} + \frac{a}{1 + b i_{mq}^2}, \qquad L_s(i_{mq}) = L_{s,0} - \frac{c i_{mq}^2}{1 + d i_{mq}^2}, \qquad M'_d(i_{mq}) = M_{d,0} - \frac{e i_{mq}^2}{1 + f i_{mq}^2} \tag{4}$$

where $L_{q,0}$, $L_{s,0}$, a, b, c, d, e, and f are the coefficients of the inductance functions. Both the self-saturation in the main-winding q-axis flux linkage as well as the cross-saturation in the suspension-winding flux linkages are modeled with the explicit functions proposed in (Yamamoto et al., 2007). Moreover, the same explicit function is applied to model the dependency of force constant M'_d on i_{mq}. The force constant M'_q is assumed to be constant throughout the operating region. When the coefficients of the explicit function are fitted to the FEA results, then the corresponding numerical values of the magnetic model are given in Table 1. The constant parameters are $L_d = 15$ mH and $M'_q = 0.66$ H/m.

As an example, Figs. 2(a), 2(b), and 2(c) show the flux-linkage maps of $\psi_{md}(i_{md})$, $\psi_{mq}(i_{mq})$, and $\psi_{sq}(i_{mq}, i_{sq})$ as function of the main-winding currents, when $i_{sd} = i_{sq} = 0.75$ A. The magnetic-model parameters are given in Table 1. Fig. 3(c) shows a flux-linkage map of $\psi_{sd}(i_{mq}, i_{sd})$ as function of suspension-winding currents, when $i_{md} = 12.5$ A and $i_{mq} = 40$ A. Fig. 4 shows a force-constant map of $M'_d(i_{mq})$ as function of main-winding currents, when $i_{sd} = i_{sq} = 0.75$ A. Based on both the flux-linkage maps and the force-constant map, it can be concluded that the proposed magnetic model agrees well with the values obtained from FEA.

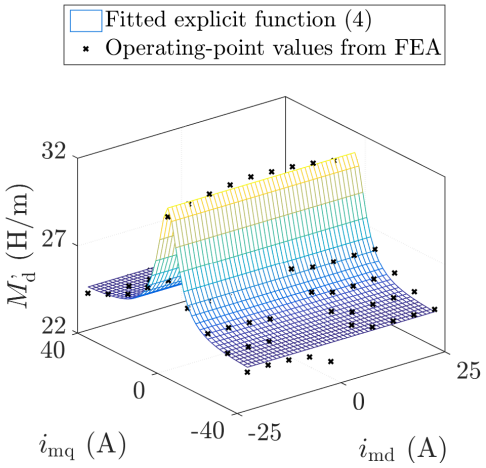

Fig. 4 Force constant $M'_{\mathrm{d}}(i_{\mathrm{md}}, i_{\mathrm{mq}})$ as function of main-winding currents, calculated with the magnetic model (4). The FEA data points are shown as black crosses.

4. Application Example: Model-Based Torque and Radial-Force Control

In this section, the proposed explicit functions are applied to design two-degrees-of-freedom (2DOF) PI-type torque and radial-force control systems for the BSyRM. It is worth keeping in mind that $\boldsymbol{u}_{\mathrm{s}}$, $\boldsymbol{i}_{\mathrm{s}}$, and $\boldsymbol{\psi}_{\mathrm{s}}$ in (1) are varying sinusoidally, with an angular frequency of ω_{M}, when the motor shaft is rotating and the radial force is produced. Thus, $\boldsymbol{u}_{\mathrm{s}}$, $\boldsymbol{i}_{\mathrm{s}}$, and $\boldsymbol{\psi}_{\mathrm{s}}$ are first transformed into their own synchronous coordinates for the suspension-winding current controller. Moreover, ideal voltage sources are assumed when designing the controllers, i.e., $\boldsymbol{u}_{\mathrm{m}} = \boldsymbol{u}_{\mathrm{m,ref}}$ and $\boldsymbol{u}_{\mathrm{s}} = \boldsymbol{u}_{\mathrm{s,ref}}$. The voltages of the main and suspension windings (in their own synchronous coordinates) are

$$\boldsymbol{u}_{\mathrm{m,ref}} = \boldsymbol{K}_{\mathrm{p,m}}(\boldsymbol{i}_{\mathrm{m,ref}} - \boldsymbol{i}_{\mathrm{m}}) + \boldsymbol{K}_{\mathrm{i,m}}\boldsymbol{x}_{\mathrm{I,m}} - \boldsymbol{R}_{\mathrm{a,m}}\boldsymbol{i}_{\mathrm{m}} + 2\omega_{\mathrm{M}}\boldsymbol{J}\boldsymbol{L}_{\mathrm{m}}\boldsymbol{i}_{\mathrm{m}} \tag{5}$$

$$\boldsymbol{u}_{\mathrm{s,ref}} = \boldsymbol{K}_{\mathrm{p,s}}(\boldsymbol{i}_{\mathrm{s,ref}} - \boldsymbol{i}_{\mathrm{s}}) + \boldsymbol{K}_{\mathrm{i,s}}\boldsymbol{x}_{\mathrm{I,s}} - \boldsymbol{R}_{\mathrm{a,s}}\boldsymbol{i}_{\mathrm{s}} + 2\omega_{\mathrm{M}}\boldsymbol{J}\boldsymbol{L}_{\mathrm{s}}\boldsymbol{i}_{\mathrm{s}} \tag{6}$$

respectively (Harnefors and Nee, 1998), where the integral states are further defined as

$$\frac{\mathrm{d}\boldsymbol{x}_{\mathrm{I,m}}}{\mathrm{d}t} = \boldsymbol{i}_{\mathrm{m,ref}} - \boldsymbol{i}_{\mathrm{m}}, \qquad \frac{\mathrm{d}\boldsymbol{x}_{\mathrm{I,s}}}{\mathrm{d}t} = \boldsymbol{i}_{\mathrm{s,ref}} - \boldsymbol{i}_{\mathrm{s}} \tag{7}$$

The reference-current vectors are denoted as $\boldsymbol{i}_{\mathrm{m,ref}}$ and $\boldsymbol{i}_{\mathrm{s,ref}}$. The controller matrices can be selected based on internal-model-control (IMC) principle

$$\boldsymbol{K}_{\mathrm{p,m}} = \alpha_{\mathrm{m}}\boldsymbol{L}_{\mathrm{m}}, \qquad \boldsymbol{K}_{\mathrm{i,m}} = \alpha_{\mathrm{m}}^2\boldsymbol{L}_{\mathrm{m}}, \qquad \boldsymbol{R}_{\mathrm{a,m}} = \boldsymbol{K}_{\mathrm{p,m}} - R_{\mathrm{m}}\boldsymbol{I} \tag{8}$$

$$\boldsymbol{K}_{\mathrm{p,s}} = \alpha_{\mathrm{s}}\boldsymbol{L}_{\mathrm{s}}, \qquad \boldsymbol{K}_{\mathrm{i,s}} = \alpha_{\mathrm{s}}^2\boldsymbol{L}_{\mathrm{s}}, \qquad \boldsymbol{R}_{\mathrm{a,s}} = \boldsymbol{K}_{\mathrm{p,s}} - R_{\mathrm{s}}\boldsymbol{I} \tag{9}$$

where α_{m} represents the bandwidth of the torque-control loop and α_{s} the bandwidth of the radial-force-control loop (Harnefors and Nee, 1998). A 2×2 identity matrix is denoted by $\boldsymbol{I}$.

4.1. Reference Calculation

The torque of the motor can be defined as

$$T_{\mathrm{M}} = 3[\psi_{\mathrm{md}}i_{\mathrm{mq}} - \psi_{\mathrm{mq}}(i_{\mathrm{mq}})i_{\mathrm{md}}] \tag{10}$$

When the motor-torque reference $T_{\mathrm{M,ref}}$ is known, then the current references $i_{\mathrm{md,ref}}$ and $i_{\mathrm{mq,ref}}$ can be solved from (10), e.g., by applying the maximum-torque-per-ampere (MTPA) principle. Alternatively, the motor may be operated with

Table 1 Explicit-Function Coefficients

Parameter	$L_{\mathrm{q,0}}$ [mH]	a [mH]	b [1/A^2]	$L_{\mathrm{s,0}}$ [mH]	c [mH/A^2]	d [1/A^2]	$M_{\mathrm{d,0}}$ [H/m]	e [H/(m · A^2)]	f [1/A^2]
Value	2.7	6	0.006	37.3	1.3	0.07	31.28	0.18	0.026

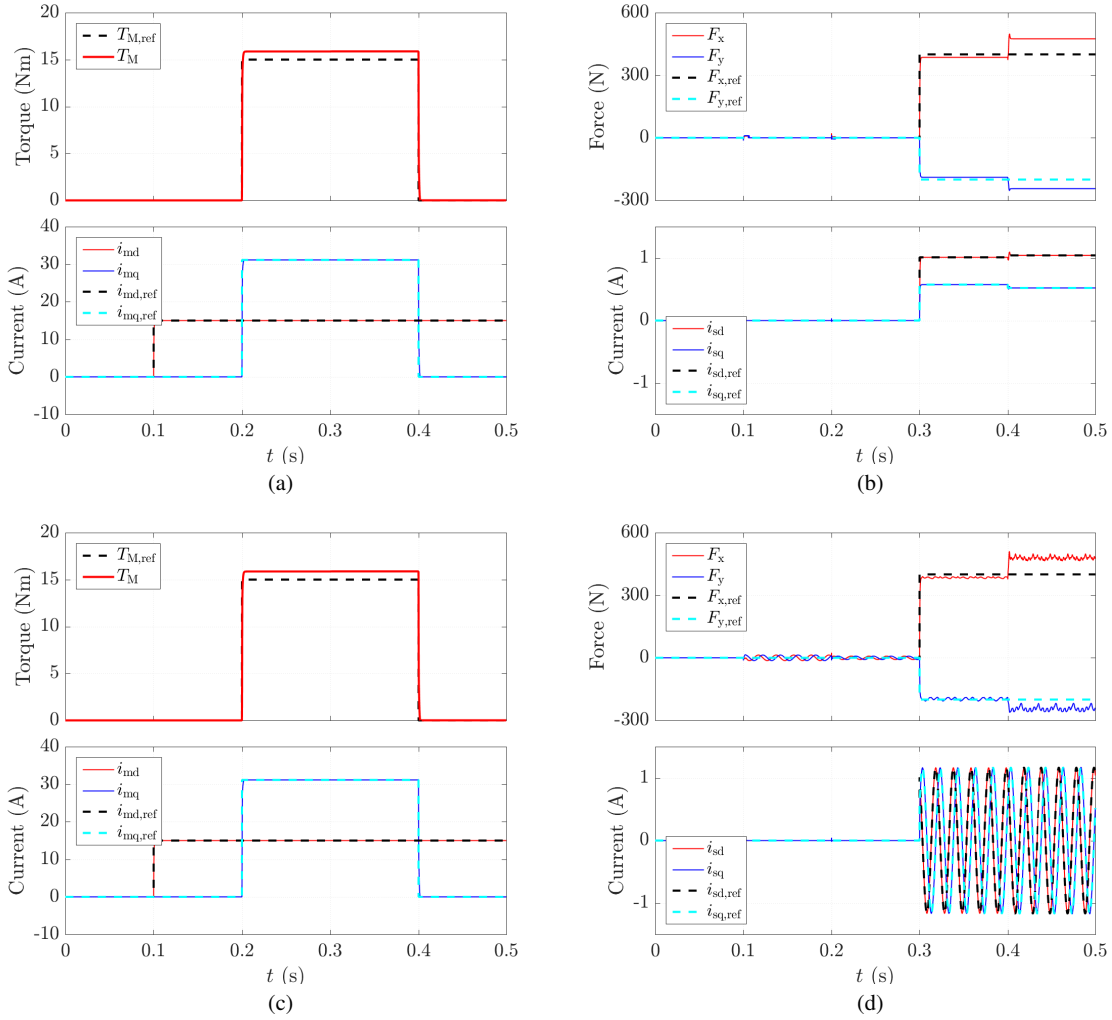

Fig. 5 Simulation result with constant magnetic-model parameters and a stand-still rotor: (a) motor torque (the first subplot) and the current components of the main winding (the second subplot); and (b) radial-force vector components (the first subplot) and the current components of the suspension winding (the second subplot). Simulation result with constant magnetic-model parameters at 3000-r/min rotor speed: (c) motor torque (the first subplot) and the current components of the main winding (the second subplot); and (d) radial-force vector components (the first subplot) and the current components of the suspension winding (the second subplot).

constant $i_{\mathrm{md,ref}}$ and $i_{\mathrm{mq,ref}}$ is then calculated from (10). Furthermore, when the reference-force vector in xy coordinates $\boldsymbol{F}^{\mathrm{s}}_{\mathrm{ref}}$ is known, then the suspension winding current references $i_{\mathrm{sd,ref}}$ and $i_{\mathrm{sq,ref}}$ can be solved from (3).

In the following simulations, the motor is operated in the torque-control mode (i.e., the torque reference is directly defined by the user). The suspension winding is operated in the force-control mode, meaning that the reference-force vector is directly defined by the user.

5. Time-Domain Simulations

The torque and the radial-force control systems, designed in previous section, are evaluated by means of time-domain simulations with two different tests. In the first test, the parameters of the magnetic model, used together with the model-based control systems, are assumed to be constant: $L_{\mathrm{d}} = 15$ mH, $L_{\mathrm{q}} = 4.3$ mH, $L_{\mathrm{s}} = 21.3$ mH, $M'_{\mathrm{d}} = 25.6$ H/m, and $M'_{\mathrm{q}} = 0.66$ H/m. In the second test, the proposed explicit-function based magnetic model is used together with the model-based control systems and the coefficients of the magnetic model are given in Table 1. The resistances of the main and suspension windings are $R_{\mathrm{m}} = 0.1\ \Omega$ and $R_{\mathrm{s}} = 2.94\ \Omega$, respectively. The bandwidths of the torque and force-control loops are $\alpha_{\mathrm{m}} = \alpha_{\mathrm{s}} = 3000$ rad/s, respectively. Both the torque controller and the radial-force controller are implemented in the continuous-time domain in these simulations.

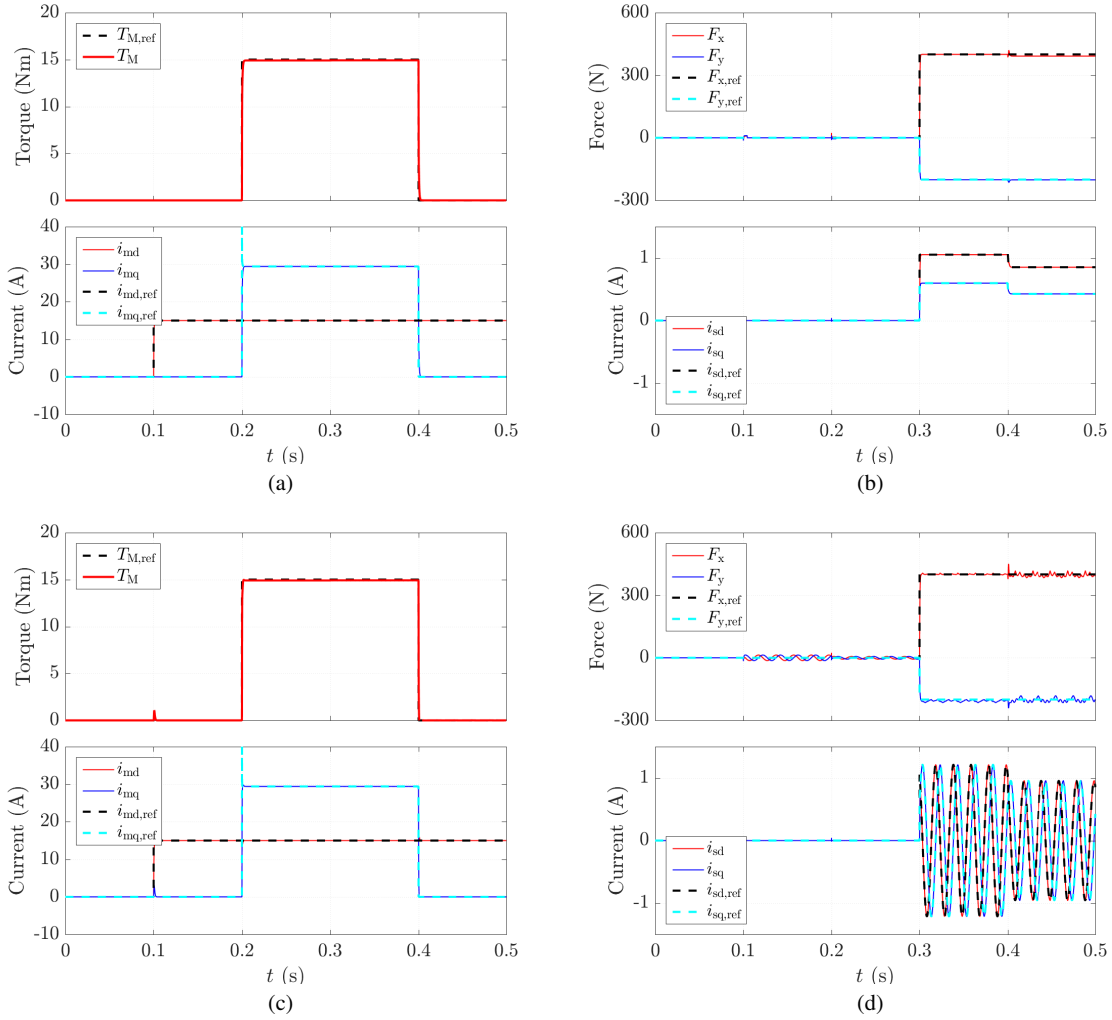

Fig. 6 Simulation result with explicit-function based magnetic-model parameters and a stand-still rotor: (a) motor torque (the first subplot) and the current components of the main winding (the second subplot); and (b) radial-force vector components (the first subplot) and the current components of the suspension winding (the second subplot). Simulation result with explicit-function based magnetic-model parameters at 3000-r/min rotor speed: (c) motor torque (the first subplot) and the current components of the main winding (the second subplot); and (d) radial-force vector components (the first subplot) and the current components of the suspension winding (the second subplot).

The following sequence is tested in the simulations with a stand-still rotor and at the rotor speed of 3000 r/min: 1) the main-winding d-axis current reference $i_{\mathrm{md,ref}}$ is stepped from 0 to 15 A @ 0 seconds; 2) the torque reference $T_{\mathrm{M,ref}}$ is stepped from 0 to 15 Nm @ 0.2 seconds and back to 0 Nm @ 0.4 seconds; 3) a radial-force reference step of $\boldsymbol{F}^{\mathrm{s}}_{\mathrm{ref}} = \begin{bmatrix} 400 & -200 \end{bmatrix}^{\mathrm{T}}$ N is applied at 0.3 seconds.

5.1. Plant Model

The plant model consists of the voltage equations (1), which are integrated in the continuous-time domain to obtain the flux linkages of both windings. Then, static mappings between the flux linkages and each current component are formed based on the FEA results as a form of four-dimensional look-up-tables (4D-LUTs). Four 4D-LUTs are required to obtain all the current components from the flux linkages. Furthermore, two additional 4D-LUTs are formed, based on the FEA results, to map the resulting current components with the radial-force components.

5.2. Results

Fig. 5 shows the simulation results, when the control system is based on the constant magnetic-model parameters. Figs. 5(a) and 5(b) show the motor torque, the radial-force components, and the corresponding current components for a stand-still rotor. Figs. 5(c) and 5(d) show the corresponding operation at the 3000-r/min rotor speed.

Fig. 6 shows the simulation results, when the control system is based on the proposed magnetic-model (4). Figs. 6(a) and 6(b) show the motor torque, the radial-force components, and the corresponding current components for a stand-still rotor. Figs. 6(c) and 6(d) show the corresponding operation at the 3000-r/min angular speed.

By comparing Figs. 5 and 6, it can be seen that the accuracies of both the torque-control loop and the radial-force control loop are clearly improved, when the control system is based on the proposed magnetic model instead of constant parameters. However, the dynamic performances of both the control loops are satisfactory even, if the control system is only based on the constant parameters.

6. Conclusions

The saturation characteristics of a double-winding BSyRM were analyzed in this paper by means of finite-element simulations. It was found out that because of the wider air gap of the motor, some of the electrical parameters of the system remain almost constant throughout reasonable operating region. However, cross-saturation between the main winding and the additional winding are clearly present even though the rotor is centric. Furthermore, it was found out that the force constants are highly dependent on the main-winding current. A simple nine-parameter magnetic model was proposed to model these non-linearities. The effectiveness of the proposed magnetic model was demonstrated by successfully applying it together with model-based torque and radial-force controllers.

References

J. Asama, Y. Hamasaki, T. Oiwa, and A. Chiba. Proposal and analysis of a novel single-drive bearingless motor. *IEEE Trans. Ind. Electr.*, 60(1):129–138, Jan. 2013.

F. Briz, M. W. Degner, and R. D. Lorenz. Dynamic analysis of current regulators for AC motors using complex vectors. *IEEE Trans. Ind. Appl.*, 35(6):1424–1432, Nov./Dec. 1999.

A. Chiba, T. Deido, T. Fukao, and M. A. Rahman. An analysis of bearingless ac motors. *IEEE Trans. Energy Convers.*, 9 (1):61–68, Mar. 1994.

W. Gruber, W. Amrhein, and M. Haslmayr. Bearingless segment motor with five stator elements: Design and optimization. *IEEE Trans. Ind. Appl.*, 45(4):1301–1308, July/Aug. 2009.

L. Harnefors and H.-P. Nee. Model-based current control of ac machines using the internal model control method. *IEEE Trans. Ind. Appl.*, 34(1):133–141, Jan./Feb. 1998.

M. Hinkkanen, H. A. A. Awan, Z. Qu, T. Tuovinen, and F. Briz. Current control for synchronous motor drives: Direct discrete-time pole-placement design. *IEEE Trans. Ind. Appl.*, 52(2):1530–1541, Mar./Apr. 2016.

C. Michioka, T. Sakamoto, O. Ichikawa, A. Chiba, and T. Fukao. A decoupling control method of reluctance-type bearingless motors considering magnetic saturation. *IEEE Trans. Ind. Appl.*, 32(5):1204–1210, Sep./Oct. 1996.

H. Mitterhofer, W. Gruber, and W. Amrhein. On the high speed capacity of bearingless drives. *IEEE Trans. Ind. Electr.*, 61(6):3119–3126, June 2014.

V. Mukherjee, J. Pippuri, A. Belahcen, S. E. Saarakkala, M. Hinkkanen, and K. Tammi. Finite element analysis for bearingless operation of a multi flux barrier synchronous reluctance motor. In *Proc. ICEMS'15*, Pattaya, Thailand, Oct. 2015.

T. Nussbaumer, P. Karutz, F. Zurcher, and J. W. Kolar. Magnetically levitated slice motors – an overview. *IEEE Trans. Ind. Appl.*, 47(2):754–766, Mar./Apr. 2011.

Z. Xu, D.-H. Lee, and J.-W. Ahn. Modeling and control of a bearingless switched reluctance motor with separated torque and suspending force poles. In *Proc. IEEE ISIE'13*, Taipei, Taiwan, May 2013.

S. Yamamoto, T. Ara, and K. Matsuse. A method to calculate transient characteristics of synchronous reluctance motors considering iron loss and cross-magnetic saturation. *IEEE Trans. Ind. Appl.*, 43(1):47–56, Jan./Feb. 2007.